applied optics

Exploring atmospheric optical turbulence: observations across zenith angles

L. F. Beesley,[1,*] J. Osborn,[1] R. Wilson,[1] O. J. D. Farley,[1] R. Griffiths,[1] and G. D. Love[2]

[1]Centre for Advanced Instrumentation, Department of Physics, Durham University, Durham DH1 3LE, UK
[2]School of Computing, Sir William Henry Bragg Building, University of Leeds, Leeds LS2 9JT, UK
*fgvp77@durham.ac.uk

Received 22 January 2024; revised 27 March 2024; accepted 2 April 2024; posted 10 April 2024; published 26 April 2024

We present measurements of the atmospheric optical turbulence as a function of zenith angle using two identical instruments, Shack-Hartmann Image Motion Monitors (SHIMMs), to measure atmospheric parameters concurrently. One instrument was pointed near zenith, while the other collected data by tracking a single star until it set and thus sampling zenith angles continuously to the horizon. By comparing these measurements, we can attribute changes in the atmospheric parameters to the changing zenith angle rather than variations in local turbulence conditions. The primary purpose of this experiment is to make comparisons between the measurements of the scintillation index, σ_I^2, and Fried parameter, r_0, with current theories. In this demonstration, we find that there is a strong agreement between the models and the instrument up until zenith angles of 70°, above which model and measurements begin to deviate. We discuss various ways in which limitations in models and our instrument may cause these deviations.

https://doi.org/10.1364/AO.519063

1. INTRODUCTION

Atmospheric optical turbulence is caused by random fluctuations in the refractive index of air, which result in the aberration of optical phase as light passes through. As the light propagates, these variations cause local focusing and defocusing leading to variations in amplitude. Generally, turbulence strength decreases with altitude with the strongest turbulence typically occurring in the ground layer [1]. As the angle from zenith increases, the length of the propagation path of light through the atmosphere increases. This elongation of the path means that the light passes through a larger volume of turbulent air, leading to greater interaction with turbulence. Consequently, the overall strength of turbulence increases with the zenith angle [2].

The relationship between the zenith angle and atmospheric parameters is well-accepted in the field of atmospheric turbulence, particularly in the context of adaptive optics. While it historically holds its relevance in astronomy, this relationship has now gained significant importance in the design and performance estimation of ground-to-satellite optical links [3–5]. This is particularly relevant for optical communications with LEO satellites, as well as for ground stations at high latitudes communicating with GEO satellites [6,7], which must operate at large zenith angles. Understanding the zenith dependency of optical light propagation through atmospheric turbulence also has relevance in satellite laser ranging, as well as solar observations [8,9].

Optical turbulence measurements were taken in September 2022 at the Roque de Los Muchachos Observatory in La Palma, Canary Islands, Spain. Here we present the measured Fried parameter (r_0) and scintillation index (σ_I^2), metrics of turbulence strength and intensity variance, respectively, measured concurrently with two identical instruments, one pointing near zenith and the other tracking a single star to slew through various zenith angles. By comparing measurements we can determine that any changes observed can be attributed to the increasing zenith angles instead of changes in the local environment caused by variations in air temperature and wind speed.

Our primary objective is to validate the leading theories of r_0 and σ_I^2 variance with zenith angle and correct for changes in zenith angle. The fact that r_0 varies with the secant of the zenith angle is one of the fundamental "laws" of adaptive optics yet this has not been experimentally tested in a direct way. Some initial studies have been conducted [10–14]—particularly in relation to scintillation, but our work differentiates itself by using a secondary instrument to eliminate temporal uncertainties in the measurements. This work serves as a demonstration to validate existing models and the experiment would need repeating for a comprehensive statistical understanding.

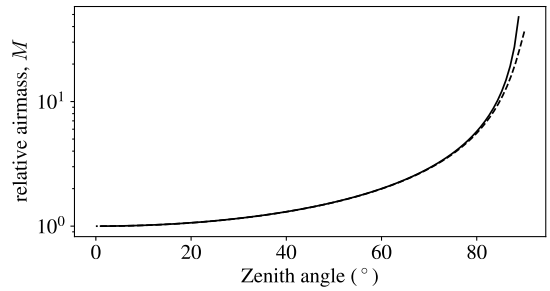

Fig. 1. Relative air mass, M, as a function of zenith angle. Lines are made using Eq. (1) and Eq. (2), solid and dashed lines, respectively. The two equations agree well up until ∼83° where the secant theory tends to infinity, and the KY theory tends to a maximum of 36.5.

2. ZENITH-DEPENDENT AIR MASS CORRECTION

The optical air mass is defined as the integrated air density over the propagating path of light. Here we will refer to the relative air mass, denoted as M. It scales the absolute air mass by dividing it by the air mass within the vertical column directly above the observer, in order to only consider the difference in the propagation path. Typically, the air mass is at its lowest value when observing at the zenith. The maximum air mass is observed when looking at a target along the horizon. If we assume a plane parallel atmospheric model and neglect the curvature of the Earth and refraction, the relative air mass is then the secant of the zenith angle, ζ:

$$M(\zeta) = \sec(\zeta). \tag{1}$$

A consequence of the $\sec(\zeta)$ dependence, however, leads to the atmospheric optical turbulence tending to be infinitely deep as the line-of-site reaches the horizon [15]. More developed models exist that take into account the geometry of the Earth and refraction of the light as it passes through a non-homogeneous atmosphere, most notably Kasten and Young's (KY) [16,17] empirical description of optical air mass, which is written as

$$M_{\mathrm{KY}}(\zeta) = \left[\cos\zeta + a \cdot (90 - \zeta + b)^{-c}\right]^{-1}, \tag{2}$$

where constants used in this formula are $a = 0.50572$, $b = 6.07995°$, and $c = 1.6364$.

Note that the two above equations only deviate at zenith values $> 80°$, as seen in Fig. 1. However, this study uses Eq. (2) to perform zenith corrections, thus eliminating any ambiguities arising from the assumptions of a flat Earth and a homogeneous atmosphere.

3. ZENITH DEPENDENCE OF ATMOSPHERIC TURBULENCE PARAMETERS

Here we review current theories and models that describe how atmospheric turbulence impacts optical propagation at different zenith angles. As this experiment employs measurements from tracking a single star we can make comparisons with theories detailing plane wave propagation. The objective of this study is to provide comparisons between theory and measurements to both assess the validity and potential limitations of the theory.

The zenith corrections expressed in the following equations are derived through geometric scaling of the vertical height above the observer, h, to the increased propagation distance resulting from the increased zenith angle, z. The adjustment is performed using

$$\begin{aligned} z &= \sec(\zeta)h, \\ dz(\zeta) &= \sec(\zeta)dh. \end{aligned} \tag{3}$$

Subsequently, we can then replace the $\sec(\zeta)$ scaling with the more appropriate $M_{\mathrm{KY}}(\zeta)$ as illustrated in Eq. (2).

A. Scintillation

There are numerous analytical approaches to modeling scintillation generated from atmospheric optical turbulence.

For weak fluctuations, the scintillation index, σ_I^2, for a plane wave is simply the Rytov variance, σ_R^2, written as [18]

$$\sigma_I^2 = \sigma_R^2 = 2.24k^{7/6}\sec^{11/6}(\zeta)\int_0^H C_n^2(h)h^{5/6}\mathrm{d}h, \tag{4}$$

where k is wavenumber $2\pi/\lambda$, H is maximum height of the considered turbulence, and $C_n^2(h)$ is the refractive index structure parameter as a function of h. This zenith relation remains the same regardless of aperture averaging.

We can modify this equation to include the more complete air mass correction shown in Eq. (2), written as

$$\sigma_R^2 = 2.25k^{7/6}M_{\mathrm{KY}}(\zeta)^{11/6}\int_0^H C_n^2(h)h^{5/6}\mathrm{d}h. \tag{5}$$

For this demonstration, our goal is to establish the relationship between σ_R^2 at zenith angle, ζ, denoted as $\sigma_R^2(\zeta)$, and σ_R^2 at the zenith, denoted as $\sigma_R^2(0)$. We achieve this by scaling them using the following expression:

$$\sigma_R^2(\zeta) = M_{\mathrm{KY}}(\zeta)^{11/6}\sigma_R^2(0). \tag{6}$$

The use of Eq. (5) is only appropriate for weak fluctuations when σ_R^2 is less than 0.3. These typically occur when the propagating wave has longer wavelengths or when the integrated atmospheric turbulence strength is weaker such as at smaller zenith angles or traveling over short propagating paths. Where we enter stronger fluctuations, an alternative theory has been suggested [20]:

$$\sigma_I^2 = \exp\left[\frac{0.49\sigma_R^2}{(1+1.11\sigma_R^{12/5})^{7/6}} + \frac{0.51\sigma_R^2}{(1+0.69\sigma_R^{12/5})^{5/6}}\right] - 1. \tag{7}$$

Figure 2 shows a comparison between the weak and strong fluctuation theories. These distributions are made using the Hufnagel-Valley turbulence distribution with the ground layer C_n^2 equal to $1.7 \times 10^{-14}\,\mathrm{m}^{-2/3}$ [19]. The wavelength is 500 nm. For this particular set of optical parameters, there is an initial agreement between the two theories up until 40°. The extent of this divergence between the two theories depends on the propagating wavelength and the specific conditions of the optical turbulence. The weak theory exhibits exponential growth as the zenith angle increases. In reality, however, scintillation reaches a point of saturation as observed in the strong fluctuation model [2,20].

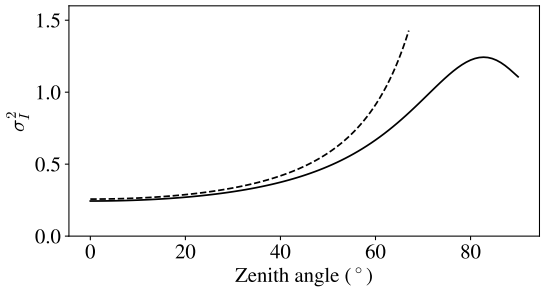

Fig. 2. Downlink scintillation index as a function of zenith angle. The dashed line uses the weak-fluctuation theory from Eq. (5), and the solid line uses the strong-fluctuation theory from Eq. (7). The turbulence distribution used here is from the H−$V_{5/7}$, where the ground layer C_n^2 is equal to 1.7×10^{-14} $m^{-2/3}$ with a wavelength of 500 nm [19].

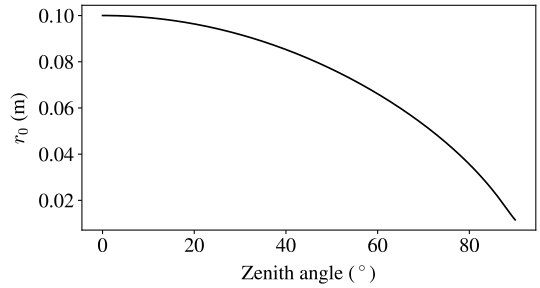

Fig. 3. Theoretical description of Fried parameter's dependence on zenith angle using Eq. (10). An r_0 of 0.1 m was used here to match the scale of the observed r_0 on the night of the measurements.

B. Fried Parameter

This paper makes use of the Fried parameter to measure the strength of turbulence-induced phase aberrations of the light. It is derived from the integrated atmospheric turbulence strength C_n^2 over the propagating path, written as [21]

$$r_0 = \left[0.423k^2 \int_0^H C_n^2(h)\mathrm{d}h\right]^{-3/5}. \tag{8}$$

The generally accepted derivation of the Fried parameter at a specific zenith angle, ζ, is given by

$$r_0(\zeta) = \sec^{-3/5}(\zeta) r_0(0), \tag{9}$$

where $r_0(0)$ is the vertical Fried parameter measured at zenith and $r_0(\zeta)$ is the Fried parameter scaled to angle ζ.

Again, as shown above, this relationship can be improved by including the Kasten and Young's air mass correction:

$$r_0(\zeta) = M_{\mathrm{KY}}(\zeta)^{-3/5} r_0(0), \tag{10}$$

where this relation is shown in Fig. 3.

4. EXPERIMENTAL DETAILS

The primary aim of this experiment is to make comparisons between turbulence measurements taken at zenith and varying zenith angles. The experiment was conducted from the roof of the Isaac Newton Telescope at the Observatorio de Los Muchachos in La Palma. Measurements were taken using a Shack-Hartmann Image Motion Monitor (SHIMM) [22,23], which uses a Shack-Hartmann wavefront sensor to measure the slopes of the wavefront at the telescope pupil plane. This set-up used a Cassegrain telescope with a 23.5 cm diameter aperture. The SHIMM itself uses a ZWO ASI462MC CMOS camera, which has a central wavelength of 695 nm. Integrated turbulence parameters like the Fried parameter can be derived from the slopes. The temporal scintillation index was determined by observing the fluctuations in the brightness of a single Shack-Hartmann spot during the measurement. The background light is derived from measuring the mean intensity in an annulus around each sub-aperture spot and this is subtracted from each measurement. 600 images of the Shack-Hartmann focal plane were taken at a rate of 100 Hz with a 2 ms exposure time (over 1 min intervals) for each measurement. The SHIMM compensates for vibrations by measuring the differential motion of spot patterns in the Shack-Hartmann focal plane. Further information on the instrument's validation can be found in [22].

Fig. 4. Two-SHIMM set-up on the roof of the Isaac Newton Telescope, La Palma.

Two SHIMMs were used in the experiment positioned approximately 2 m apart, seen in Fig. 4. The primary SHIMM, referred to as SHIMM1, measured the integrated turbulence parameters for targets with zenith angles smaller than 20°. Within this range, Eqs. (5) and (10) were confidently employed to perform air mass correction up to zenith. The secondary SHIMM, which we refer to as SHIMM2, tracked Vega from near zenith down to near 90° zenith angle. By comparing the measurements taken by SHIMM1 and SHIMM2, the validity of Eqs. (7) and (9) at all zenith angles could be tested.

5. RESULTS

Here we present measurements of both σ_I^2 and r_0 for the two SHIMMs, where one is at zenith and the other at varying zenith angles. We then scale SHIMM1 data to SHIMM2's zenith angle following the theory presented in the previous sections.

Figure 5 shows the images taken by both SHIMMs concurrently at 6° and 89° zenith. With increasing zenith angle there is an increased spatial variance in the spot brightness across the Shack-Hartmann focal plane. There is also an overall mean reduction in the received intensity across the aperture. We also observe more temporal variations in the spot brightness as we increase in zenith angle. All these effects are as expected.

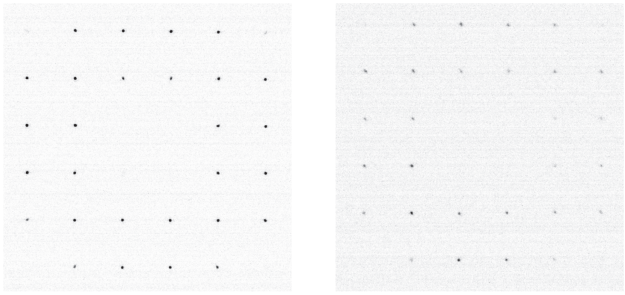

Fig. 5. Shack-Hartmann spot pattern for two measurements at zenith angles of (a) 6° and (b) 89°. The data was taken over a 2 ms exposure, and these measurements were taken simultaneously at 03:09 AM. Both images have been plotted on the same greyscale range.

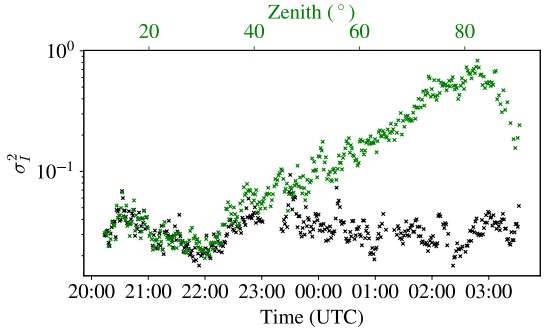

Fig. 6. Measured σ_I^2 data from SHIMM1 (black) and SHIMM2 (green) as a function of time and zenith angle of SHIMM2. SHIMM1 stayed within 20° of zenith whereas SHIMM2 tracked Vega from 10° to the horizon at 90°. The secondary x-axis shows the zenith angle of SHIMM2. All data points represent the average of a minute of data. All data is scaled to 500 nm.

Our results from this demonstration found that when observing at similar zenith angles for the first half of the night, the measurements of both atmospheric parameters yield very close values, serving as a means of validating the two instruments. Further analysis of the relationship between the two SHIMM measurements is shown below.

A. Scintillation Index

Figure 6 shows the measured σ_I^2 by SHIMM1 and SHIMM2 throughout the night of the 21st. The local σ_I^2 mean, which we measure from zenith, is 0.03, which varied between 0.02 and 0.08. The σ_I^2 measured by SHIMM2 reaches saturation at 02:50 AM, which occurs at 80° zenith, which is similar to the zenith angle predicted by theory [2].

Figure 7 shows the measured σ_I^2 of SHIMM2 compared with SHIMM1, which measures the optical turbulence at zenith and is scaled to SHIMM2's corresponding zenith angle using Eq. (7). Here it is seen that there is a very good agreement between both the weak and strong fluctuation models and the measured σ_I^2 up until ∼80°, before this the data has a correlation coefficient of 0.91. Beyond this zenith angle, the weak fluctuation asymptotically increases, and the strong fluctuation theory begins to saturate; however this model estimates the measured σ_I^2 to be higher than the observed σ_I^2. A closer view

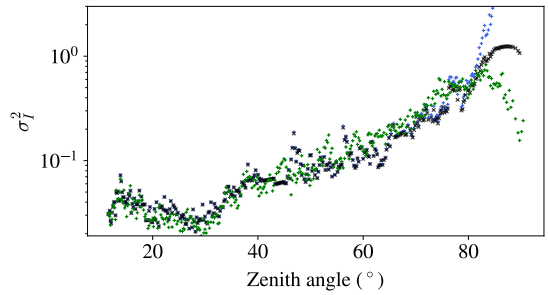

Fig. 7. Comparisons between measured σ_I^2 and theoretically derived σ_I^2 across varying zenith angles are presented. Green crosses represent direct measurements from SHIMM2, while blue and black crosses correspond to weak and strong fluctuation theories, respectively, using Eqs. (5) and (7), both derived from SHIMM1 and subsequently scaled to the corresponding zenith angle of SHIMM2.

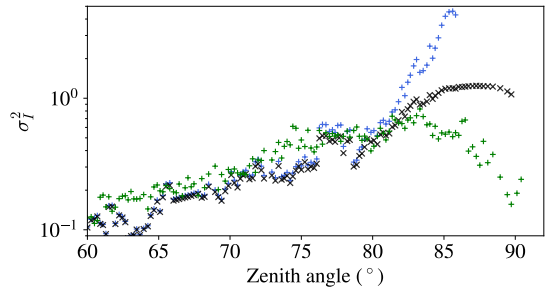

Fig. 8. Zoom-in of Fig. 7 at very large zenith angles.

of the point of deviation between all three datasets is shown in Fig. 8.

There are several potential reasons for the divergence between the model and measurements at very large zenith angles. Since the model, as represented in Eq. (7), accounts for strong fluctuations, we hypothesize that the reduction in scintillation is attributed to alternative atmospheric effects, such as ray bending due to refraction or an increase in atmospheric attenuation, which is not incorporated into the models.

Unfortunately, it is difficult to disentangle instrumental effects from optical turbulence effects especially when observing at very large zenith angles. Despite this, this demonstration indicates that we can estimate σ_I^2 up to 80° from an instrument pointed near zenith in this particular environment. Further studies will be necessary to comprehend the nuances behind the observed disagreement at very large zenith angles.

B. Fried Parameter

Figure 9 shows the r_0 measured by SHIMM1 and SHIMM2 over the 7 h run. SHIMM1, which pointed toward zenith, shows that throughout the night the Fried parameter reduces from 15 to 5 cm, indicating that the optical turbulence is getting stronger throughout the night. This reduction in r_0 may be attributed to an increase in local temperature and wind. Additionally, this trend is not observed in the measured scintillation, which decreases throughout the night; therefore we can attribute this change to low-altitude turbulence.

Additional comparisons between the two measurements are presented in Fig. 10. Here we compare the data measured

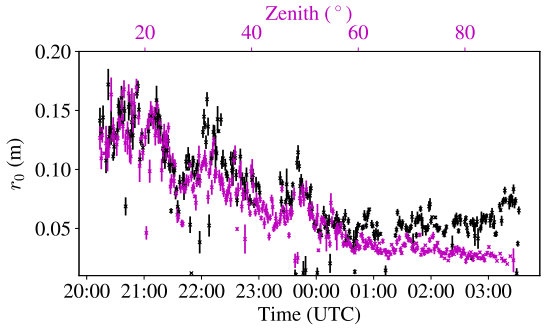

Fig. 9. Measured r_0 data from SHIMM1 (black) and SHIMM2 (purple) as a function of time and zenith angle of SHIMM2. SHIMM1 is scaled at zenith whereas SHIMM2 remains unscaled, representing the measured r_0 at that zenith angle. All data points are the average of a minute of data taken over a 7 h run. The secondary x-axis shows the zenith angle of SHIMM2. All data is scaled to 500 nm.

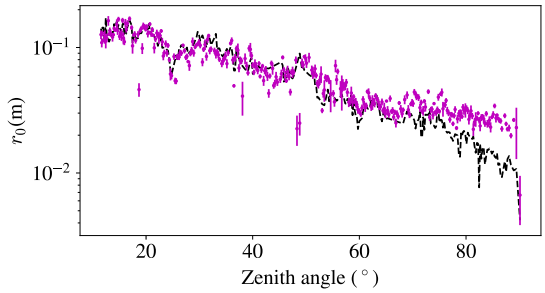

Fig. 10. Comparison between the measured r_0 and r_0 derived from existing theory. (Purple) r_0 measured by SHIMM2 across a range of zenith angles, (black) r_0 derived from measurements taken by SHIMM1 at zenith and then scaled to the corresponding zenith angle using Eq. (10). All data points are scaled to 500 nm and averaged over a minute of data.

by SHIMM2 obtained across varying zenith angles with data collected by SHIMM1 at zenith and then scaled to SHIMM2's corresponding zenith angle using the theory described in Eq. (10). Scaling is performed by multiplying SHIMM1 data by $M_{\mathrm{KY}}(\zeta)^{-3/5}$ for each zenith angle. We observe a strong agreement between measurement and theory up until 70°, at which point the two datasets begin to diverge. For zenith angles beyond this threshold, both Kasten and Young's theory and secant scaling overestimates r_0 suggesting the turbulence strength is weaker than the model predicts.

Our primary belief is that this mismatch arises from the omission of optical propagation effects in Eq. (8), as it is solely a linear sum of all air masses along the propagation path. We have observed in simulation that the optical propagation causes an increase in the measured r_0. We believe that this is not an instrumental error due to a small r_0, as the SHIMM is capable of measuring r_0 values down to 1 cm, as seen in [22].

6. CONCLUSION

The main goal of this experiment was to compare turbulence measurements obtained at zenith with those measured at varying zenith angles to check the limitations of Eqs. (7) and (10). The experiment ran on the 21st of September, 2022, on the roof of the Isaac Newton Telescope at the Roque de Los Muchachos Observatory in La Palma, Canary Islands, Spain. This study made comparisons between the turbulence parameters at zenith and at varying zenith angles by using two identical SHIMMs that ran concurrently in close proximity. This served to mitigate potential ambiguities in our measurements that could arise from local fluctuations in the turbulence conditions.

The results indicate that the measured scintillation index (σ_I^2) and Fried parameter (r_0) only began to diverge from their respective models at large zenith angles. For σ_I^2, a strong alignment is observed with both weak and strong fluctuation theories [Eqs. (5) and (7)] until zenith angles surpass ∼85°. Beyond this point, weak fluctuations increase asymptotically, and strong fluctuations saturate, both estimating a higher σ_I^2 compared to the observed values. We believe the primary reason for the discrepancy is that Eq. (7) does not explicitly incorporate certain atmospheric effects. These effects include refraction-induced ray bending, increased atmospheric attenuation, and the influence of uncorrelated turbulence occurring at a distance. However, this study successfully demonstrates that one can estimate σ_I^2 to large zenith angles, for this particular environment, by using a measurement taken near zenith. Further studies are required to understand the nuances causing discrepancies at very large zenith angles.

Similarly, r_0 aligns well with the theory up to a zenith angle of ∼70°. At larger zenith angles, both Kasten and Young's theory and secant scaling overestimates r_0 indicating weaker turbulence than these models predict. We attribute this discrepancy to the omission of optical propagation effects in Eq. (10).

Disentangling instrumental effects from optical turbulence remains challenging, especially during observations at very large zenith angles. Despite these challenges, we believe that for this particular turbulent environment, Eqs. (7) and (10) can be confidently used to calculate the atmospheric turbulence parameters within these limits. Consequently, a SHIMM can be employed in any astronomical site as a monitor and the measured turbulence parameters can be extrapolated to a zenith angle as low as ∼70°.

Funding. UK Research and Innovation (MR/X015106/1); Engineering and Physical Sciences Research Council (EP/T518001/1).

Acknowledgment. The authors would like to thank the Instituto de Astrofisica de Canarias (IAC) for providing access to the observation site. The results presented in this paper make use of NumPy [24], Matplotlib [25], Python [26], and pandas [27].

Disclosures. The authors declare no conflicts of interest.

Data availability. Data underlying the results presented in this paper are not publicly available at this time but may be obtained from the authors upon reasonable request.

REFERENCES

1. T. Butterley, R. W. Wilson, M. Sarazin, *et al.*, "Characterization of the ground layer of turbulence at Paranal using a robotic SLODAR system," Mon. Not. R. Astron. Soc. **492**, 934–949 (2020).
2. F. Roddier, "The effects of atmospheric turbulence in optical astronomy," Prog. Opt. **19**, 281–376 (1981).
3. R. L. Phillips, L. C. Andrews, R. L. Phillips, *et al.*, "Scintillation model for a satellite communication link at large zenith angles," Opt. Eng. **39**, 3272–3280 (2000).

4. M. Chen, C. Liu, D. Rui, *et al.*, "Performance verification of adaptive optics for satellite-to-ground coherent optical communications at large zenith angle," Opt. Express **26**, 4230–4242 (2018).
5. L. B. Stotts and L. C. Andrews, "Bit error rate performance of a laser ground-to-satellite uplink communications systems in the presence of atmospheric turbulence and loss," in *IEEE International Conference on Space Optical Systems and Applications, ICSOS* (2022), pp. 66–73.
6. E. Fischer, M. Feriencik, K. Kudielka, *et al.*, "Upgrade of ESA optical ground station with adaptive optics for high data rate satellite-to-ground links," in *IEEE International Conference on Space Optical Systems and Applications, ICSOS* (2017), p. 63.
7. W. Chen, J. Sun, X. Hou, *et al.*, "5.12 Gbps optical communication link between LEO satellite and ground station," in *IEEE International Conference on Space Optical Systems and Applications, ICSOS* (2017), pp. 260–263.
8. D. Vasylyev, W. Vogel, and F. Moll, "Satellite-mediated quantum atmospheric links," Phys. Rev. A **99**, 053830 (2019).
9. J. Marino, "Expected performance of solar adaptive optics in large-aperture solar telescopes," Opt. Eng. **51**, 101709 (2012).
10. A. T. Young, "Saturation of scintillation," J. Opt. Soc. Am. **60**, 1495–1500 (1970).
11. G. Parry, J. G. Walker, and R. J. Scaddan, "On the statistics of Stellar speckle patterns and pupil plane scintillation," Opt. Acta **26**, 563–574 (1979).
12. B. H. Briggs and I. A. Parkin, "On the variation of radio star and satellite scintillations with zenith angle," J. Atmos. Terr. Phys. **25**, 339–366 (1963).
13. H. J. Chivers and R. D. Davies, "A comparison of radio star scintillations at 1390 and 79 Mc/s at low angles of elevation," J. Atmos. Terr. Phys. **24**, 573–584 (1962).
14. S. Solomon, A. L. Schmeltekopf, and R. W. Sanders, "On the interpretation of zenith sky absorption measurements," J. Geophys. Res. Atmos. **92**, 8311–8319 (1987).
15. A. T. Young, "Air mass and refraction," Appl. Opt. **33**, 1108–1110 (1994).
16. F. Kasten, "A new table and approximation formula for the relative optical air mass," Arch. Meteorol. Geophys. Bioklimatol. **14**, 206–223 (1965).
17. F. Kasten and A. T. Young, "Revised optical air mass tables and approximation formula," Appl. Opt. **28**, 4735–4738 (1989).
18. E. L. Bass, "Aperture averaging of optical scintillations based on a spectrum with high wave number bump," Opt. Eng. **34**, 26–31 (1995).
19. L. C. Andrews, R. L. Phillips, D. Wayne, *et al.*, "Near-ground vertical profile of refractive-index fluctuations," Proc. SPIE **7324**, 732402 (2009).
20. L. C. Andrews, R. L. Phillips, C. Y. Hopen, *et al.*, "Theory of optical scintillation," J. Opt. Soc. Am. A **16**, 1417–1429 (1999).
21. R. Tyson, *Principles of Adaptive Optics* (Elsevier, 1991).
22. R. Griffiths, J. Osborn, O. Farley, *et al.*, "Demonstrating 24-hour continuous vertical monitoring of atmospheric optical turbulence," Opt. Express **31**, 6730–6740 (2023).
23. S. Perera, R. W. Wilson, J. Osborn, *et al.*, "SHIMM: a seeing and turbulence monitor for astronomy," Proc. SPIE **9909**, 99093J (2016).
24. C. R. Harris, K. J. Millman, S. J. van der Walt, *et al.*, "Array programming with NumPy," Nature **585**, 357–362 (2020).
25. J. D. Hunter, "Matplotlib: a 2D graphics environment," Comput. Sci. Eng. **9**, 90–95 (2007).
26. G. Van Rossum and F. L. Drake, *Python 3 Reference Manual* (CreateSpace, 2009).
27. W. McKinney, "Data structures for statistical computing in Python," in *Proceedings of the 9th Python in Science Conference* (2010), Vol. **1**, p. 56.